Ocean Systems Engineering, *Vol. 11, No. 1 (2021) 1-16*
DOI: https://doi.org/10.12989/ose.2021.11.1.001

Experimental and numerical investigation of a surface-fixed horizontal porous wave barrier

Sunny Kumar Poguluri[a], Jeongrok Kim[b], Arun George[c] and I.H. Cho[*]

Department of Ocean System Engineering, Jeju National University, Jeju 690-756, Republic of Korea

(Received December 22, 2020, Revised January 19, 2021, Accepted January 24, 2021)

Abstract. Experimental and numerical investigations were conducted to study the performance of a surface-fixed horizontal porous wave barrier in regular waves. The characteristics of the reflection and transmission coefficients, energy dissipation, and vertical wave force were examined versus different porosities of the barrier. Numerical simulations based on 3D Reynolds Averaged Navier-Stokes equations with standard *low-Re k-ε* turbulent closure and volume of fluid approach were accomplished and compared with the experimental results conducted in a 2D wave tank. Experimental measurements and numerical simulations were shown to be in satisfactory agreement. The qualitative wave behavior propagating over a horizontal porous barrier such as wave run-up, wave breaking, air entrapment, jet flow, and vortex generation was reproduced by CFD computation. Through the discrete harmonic decomposition of the vertical wave force on a wave barrier, the nonlinear characteristics were revealed quantitatively. It was concluded that the surface-fixed horizontal barrier is more effective in dissipating wave energy in the short wave period region and more energy conversion was observed from the first harmonic to higher harmonics with the increase of porosity. The present numerical approach will provide a predictive tool for an accurate and efficient design of the surface-fixed horizontal porous wave barrier.

Keywords: energy dissipation; experiments; surface-fixed horizontal porous barrier; vertical wave force; wave reflection; wave transmission

1. Introduction

The traditional gravity-type breakwaters offer many advantages in preventing incoming waves but suffer from the settlement problem due to their self-weight and soft seabed. The horizontal wave barrier located below or on the free surface could be one of the possible alternatives of breakwaters by dissipating the incoming wave energy, resultingly reducing the transmitted waves. If installed in front of the seawall, it can help reduce the wave oscillation inside the marinas and harbor, consequently avoid broken mooring lines, damaged fenders, hazards in berthing. The greatest advantage of the horizontal barrier lies in allowing the free exchange of seawater or migration of

*Corresponding author, Professor, E-mail: cho0904@jejunu.ac.kr
[a] Ph.D., E-mail: sunnykumar@jejunu.ac.kr
[b] Ph.D., E-mail: wodqks1005@jejunu.ac.kr
[c] Ph.D. Student, E-mail: arunmvgeorge@jejunu.ac.kr

http://www.techno-press.org/?journal=ose&subpage=7 ISSN: 2093-6702 (Print), 2093-677X (Online)

marine animals for the benefit of the environment. Numerous studies are widely available in the past literature, owing to the interest in inherent characteristics of the horizontal barrier. Especially, the perforated/porous barriers can enhance the effectiveness in reducing the wave loads on the barrier and improving the effect of wave energy dissipation (Chwang and Chan 1998, Yu 2002).

In the framework to study the effectiveness of the horizontal porous barrier in waves, theoretical studies, numerical modellings, and experimental works are widely used approaches. The theoretical efforts have been mainly focused on deriving the relationship between the pressure difference and the fluid passing velocity at the porous boundary (Siew and Hurley 1977) to consider the energy dissipation. Some of the researchers have proposed a linear-relation model, called Darcy's law (Yu and Chwang 1994, Cho and Kim 2008, Liu and Li 2011, Evans and Peter 2011, An and Faltinsen 2012), and some adopted a quadratic-relation model as a porous boundary condition (Mei *et al*. 1974, Laws and Livesey 1978, Molin 1992, Yu 1995, Molin and Nielsen 2004, Molin *et al*. 2008, Molin 2001, Crowley and Porter (2012), An and Faltinsen 2012, Poguluri and Cho 2020). The existing analytical approaches and potential-based numerical models (Boussinesq and shallow water equations) cannot explain the complex wave interaction with the porous barrier completely. These interactions involve wave breaking, jet flow through the small openings, free-surface fragmentation, air entrapment, and effects of fluid turbulence. To address the detailed and intense interactions of complex flow physics between wave and porous barrier, the 3D turbulent model is needed together with experimental tests.

The application of the computational fluid dynamics (CFD) model for the two-phase flow problem can provide the detailed description of the flow behavior past the horizontal porous barrier. Seiffert *et al*. (2014) computed the vertical force on the horizontal plate by solitary wave using Open Field Operation and Manipulation (OpenFOAM) based on InterFoam including Volume of Fluid (VOF); notably, they ignored the effect of viscosity. Nonlinear interaction of the submerged horizontal plate with solitary wave was investigated by the Constrained interpolation profile (CIP)-based Cartesian grid method using VOF method; it was then compared with the experimental results involving different wave heights and submergence depths (You *et al*. 2019). They presented important nonlinear wave characteristics such as vortex evolution, wave breaking, and air entrapment. Poguluri and Cho (2020) studied a horizontal slotted plate with a vertical seawall as wave absorber through analytical and numerical approaches. Reynolds averaged Navier-Stokes (RANS) based CFD solution was used to estimate the variation of reflection coefficient, vertical force on the slotted plate, wave run-up, and horizontal force on the vertical wall for different submergence depths, porosities, plate lengths, and wave steepnesses. Their numerical results were compared with the analytical solutions based on the matched eigenfunction expansion method. The numerical results showed that by decreasing the plate submergence depth, the generation of higher harmonic waves and the inception of wave breaking are promoted. It was reported that the small-scale vortices and tip-vortex at both ends exist with different degrees of generation depending on the porosity of the horizontal plate. In total, the results predicted by the analytical solutions were satisfactory and consistent with the CFD results.

The present study aims to analyze the energy-dissipation effect of a surface-fixed horizontal porous barrier by investigating the reflection and transmission coefficients, and vertical wave forces on the porous barrier. For this, we conducted experiments in a 2D wave tank and numerical simulations based on CFD using STAR-CCM+ by changing barrier porosity and wave characteristic. In particular, to understand the complex flow physics, the qualitative behavior of complex waves propagating over the horizontal barrier with different porosities including wave breaking, free surface fragmentation, air entrapment, jet flow, and vortex generation were also addressed using

CFD simulation. The time series of the vertical wave force from the CFD were given, and the degree of nonlinearity of the wave force was presented quantitatively by the harmonic-decomposition method. The analytical solutions on a surface-fixed rigid barrier by Linton (2001) were used to validate the CFD solution along with experimental results. Finally, the paper highlights some of the conclusions of the results obtained through experimental measurement and numerical calculations.

2. Experimental wave tank

The experiments were carried out in a 2D wave tank (0.8 m wide, 1.0 m deep, and 20 m long) at Jeju National University. The piston-type wavemaker at one end of the tank can be operated to generate waves by a user-defined time-voltage input. The inclined porous wave absorbing system was equipped at the other end to efficiently reduce the reflected waves. The water depth is maintained at 0.6 m.

2.1 Experimental setup

The horizontal porous barrier model is a punched steel plate with circular holes arranged in a staggered manner as shown in Fig. 1(a). A plate is punched uniformly with the fixed circular hole of diameter ($2r$) 3 mm and the center to center distance of adjacent holes (c) is 6, 8, and 12 mm, which correspond to the barrier porosities (P) of 0.2267, 0.1275, and 0.0567, respectively (see Fig. 1(a)). The barrier was fixed on the free surface with the help of four vertical steel rods attached to the wave tank (Fig. 1(b)). To obtain the wave reflection and transmission coefficients, three wave probes on the wave generation side and one wave probe at the lee side of the model are installed. The first wave probe (WP1) is fixed at 2.55 m from the barrier front and the spacing of the second (WP2) and the third (WP3) was set to 0.175 and 0.768 m from the first gauge, respectively. The lee side wave probe (WP4) is at 1 m from the barrier. The location and spacing between wave probes are selected to avoid singularities in the separation process of incident and reflected waves. Fig. 1 presents a schematic view of the porous barrier and positions of the wave probes in the wave tank. The measured wave elevation data from the wave probes were fed to the wave frequency amplifier. Then, the data logger is used to store them into the computer for further analysis. The noise from the data is removed using a low-pass filter.

3. Numerical modeling

To simulate nonlinear wave-structure interaction, the flow of an incompressible viscous fluid is governed by the continuity and Reynolds averaged Navier-Stokes equations as follows

$$\frac{\partial u}{\partial x}+\frac{\partial v}{\partial y}+\frac{\partial w}{\partial z}=0 \tag{1}$$

$$\frac{\partial u}{\partial t}+u\frac{\partial u}{\partial x}+v\frac{\partial u}{\partial y}+w\frac{\partial u}{\partial z}=-\frac{\partial p}{\partial x}+(\nu_t+\nu)\nabla^2 u+\frac{\partial}{\partial x}\left(\nu_t\frac{\partial u}{\partial x}\right)+\frac{\partial}{\partial y}\left(\nu_t\frac{\partial v}{\partial x}\right)+\frac{\partial}{\partial z}\left(\nu_t\frac{\partial w}{\partial x}\right)-\frac{2}{3}\frac{\partial k}{\partial x},$$

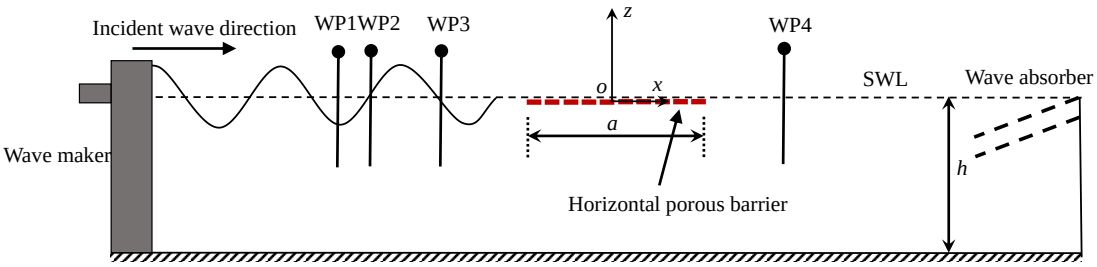

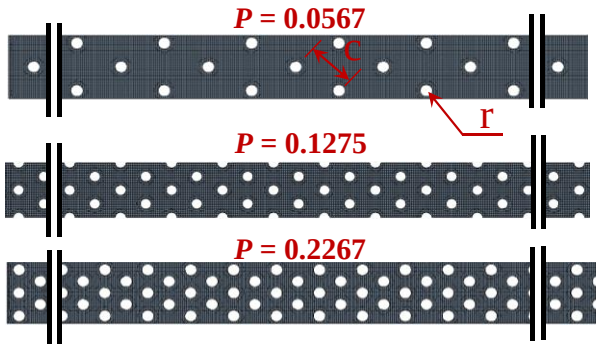

Where,

h :	Water depth
a :	Barrier length
c :	Center to center spacing
r :	Radius of the hole
WP :	Wave probes
SWL :	Still water level

(a)

(b)

Fig. 1 (a) Schematic view of the experimental setup of a porous barrier in a wave tank (b) Snapshot of the installation of a porous barrier in a wave tank

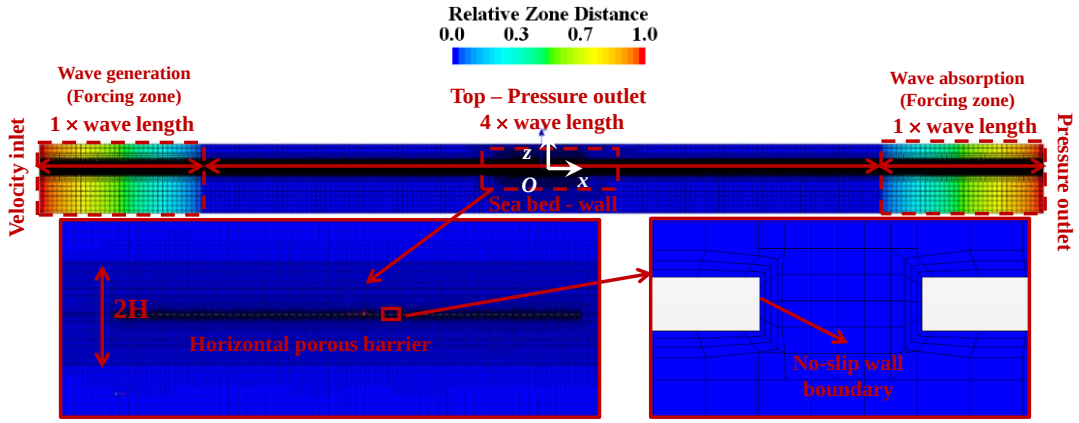

Fig. 2 Computational domain with boundary conditions and mesh details close to porous barrier (*H*: wave height)

$$\frac{\partial v}{\partial t}+u\frac{\partial v}{\partial x}+v\frac{\partial v}{\partial y}+w\frac{\partial v}{\partial z}=-\frac{\partial p}{\partial y}+(\nu_t+\nu)\nabla^2 v+\frac{\partial}{\partial x}\left(\nu_t\frac{\partial u}{\partial y}\right)+\frac{\partial}{\partial y}\left(\nu_t\frac{\partial v}{\partial y}\right)+\frac{\partial}{\partial z}\left(\nu_t\frac{\partial w}{\partial y}\right)-\frac{2}{3}\frac{\partial k}{\partial y},$$

$$\frac{\partial w}{\partial t}+u\frac{\partial w}{\partial x}+v\frac{\partial w}{\partial y}+w\frac{\partial w}{\partial z}=-\frac{\partial p}{\partial z}+(\nu_t+\nu)\nabla^2 w+\frac{\partial}{\partial x}\left(\nu_t\frac{\partial u}{\partial z}\right)+\frac{\partial}{\partial y}\left(\nu_t\frac{\partial v}{\partial z}\right)+\frac{\partial}{\partial z}\left(\nu_t\frac{\partial w}{\partial z}\right)-\frac{2}{3}\frac{\partial k}{\partial z}+g\,. \qquad (2)$$

where u, v and w are the velocity components; p denotes the pressure; g is the acceleration due to gravity; k the turbulent kinetic energy; ν molecular viscosity; and ν_t eddy viscosity. To estimate the eddy viscosity, a standard *low-Re k* and ε (turbulent dissipation) model is adopted.

A 3D numerical wave tank (NWT) simulations were performed as illustrated in Fig. 2, where Cartesian coordinate frame of reference (*Oxyz*) has been selected, origin located at the center of the porous barrier, x in the wave propagation direction, and vertical oscillations in the z-direction with still water level (SWL) at $z=0$. To enable long-time simulations, an effective wave generation and absorption in a small computation domain of NWT is needed without compromising the accuracy. The present study applied a gradual forcing solution theoretically at the generation and reflection boundaries (Enger *et al*. 2014, Peric 2017). The initial free-surface elevation and velocity of the incident wave are applied using the 5th-order Stokes wave solution. To reduce the computational time, the initial free-surface elevation in the NWT was activated to the boundary which exactly ends at the front tip of the barrier. NWT is governed by four different types of boundary conditions imposed on the inlet with velocity-inlet, outlet and top as pressure outlet; bottom and barrier as wall with no-slip condition; and sides as symmetric boundary condition. The primary work of the present study is to deal with the violent free surface behavior associated with wave breaking, multiple small jets and vortices formation. To handle these complex wave evolution, an accurate sharp free surface interface tracking is needed. Thus, the VOF method combined with a high-resolution interface capturing scheme (HRIC) is adopted.

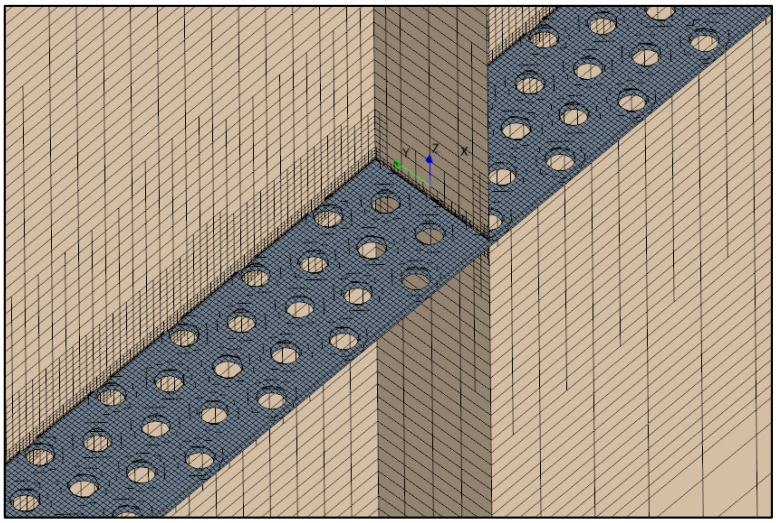

Fig. 3 Closer view of mesh distribution near free-surface and porous barrier based on Mesh-type 2

4. Results and discussion

4.1 Numerical convergence test

The performance assessment of the surface-fixed horizontal porous barrier exposed to incoming waves often requires nonlinear analysis because of complex wave-structure interactions. Accurate numerical estimation of wave loads and wave interactions is to be evaluated for an efficient design of the horizontal porous barrier. Accordingly, a convergence test was initially carried out depending on parameters, such as mesh size, to ascertain the obtainable degree of accuracy. For the validation of CFD solutions, they were compared with experimental results following the details provided in Section 3. The automatic convective Courant–Friedrichs–Levy (CFL) time step was adopted to ensure a sufficient time step throughout the simulations by adjusting the overall Courant number in the full computational domain with a mean value of 0.3 and maximum value of 0.5. The description of the interface is based on the VOF with two fluids such as water (1,000 kg/m^3) and air (1.184 kg/m^3) along with HRIC (angle factor = 0.05). To achieve a steady-state solution for waves with a longer period, a second-order unsteady implicit scheme and an up-wind scheme for the time and space were used, respectively. The initial wave profile was defined with the 5th-order Stokes wave.

The NWT of total length $6\times\lambda$ (where λ is wavelength) were selected. For effective wave generation, wave forcing was gradually applied with the theoretical solution over a specified region of the NWT with the square of the cosine function as shown in Fig. 2 (as relative zone distance). The computational domain was divided into finite volume grids with a constant base size using the surface remesher, trimmer cell mesher, and prism layer mesher. To enable effective mesh distribution, refinements at the free surface, porous barrier, and boundary layer were performed using the respective details given in Table 1 and the typical mesh based on Mesh type 2 shown in Fig. 3

Table 1 Details of grid convergence tests

Type	Boundary layer ($y+ < 3$)		Mesh refinement		Total number of cells
	Prism layer		Free surface	Porous barrier	
	Thickness	1st cell distance			
Mesh 1	0.003	3	$\Delta x/\Delta z$, $\Delta y/\Delta z$ = 4 and H/6,	$\Delta x, \Delta y$ and $\Delta z = 0.003$	790,376
Mesh 2	0.0015	3	$\Delta x/\Delta z$, $\Delta y/\Delta z$ = 4 and H/10,	$\Delta x, \Delta y$ and $\Delta z = 0.0015$	1,083,404
Mesh 3	0.001	3	$\Delta x/\Delta z$, $\Delta y/\Delta z$ = 2 and H/15,	$\Delta x, \Delta y$ and $\Delta z = 0.001$	3,504,171

The porous barrier with porosity P of 0.2257, length a of 0.8 m, and thickness of 2 mm was chosen for the grid convergence testing. The 5th-order Stokes wave was generated with the wave period T = 1.6 sec. and wave steepness $H/\lambda = 0.02$. Fig. 4 shows the time history of the free-surface elevation at positions (WP1, WP2, WP3, and WP4) along with the experimental results distinguished in a solid line. Notably, the computational free-surface elevation using Mesh-types 2 and 3 shows good agreement with the experimental measurement than Mesh-type 1. The results show good convergence at the finer mesh-structure. Consequently, Mesh-type 2 was used for the rest of the simulation.

4.2 CFD validation

The numerical validation was conducted at the selected wave parameters and barrier properties as given in Table 2. The accuracy of the adopted numerical CFD model should be ascertained by comparing a variety of simulations. First, the time history of free-surface wave elevations between the measurement and calculation at four different positions (i.e., WP1, WP2, WP3, and WP4) were compared in Fig. 5. Notable agreements between them demonstrate the feasibility of the present numerical model for the complex free-surface profile past the rigid (case 1) and porous (case 2) model.

For the separation of incident and reflected waves, a 3-probes (WP1, WP2, and WP3) method based on the least square technique was adopted (Mansard and Funke 1980). While the incident wave passes through the surface-fixed horizontal porous barrier, some parts of wave energy lost through the viscosity of water and air using the mechanism of friction, vortex formation, jet flow, and wave breaking. Accordingly, the reflected and transmitted waves are reduced partly by the porous barrier. The reflection and transmission coefficients have been obtained from the wave data for the selected time range as given in Fig. 5. Table 3 summarizes the respective values of cases 1 and 2 of reflection and transmission coefficients. The reflection coefficient from the experimental analysis is 4% and 2% more, whereas the transmission coefficients are 2% more and 6% less in

cases 1 and 2, respectively compared with the CFD results. On the overall, two results showed satisfactory agreements.

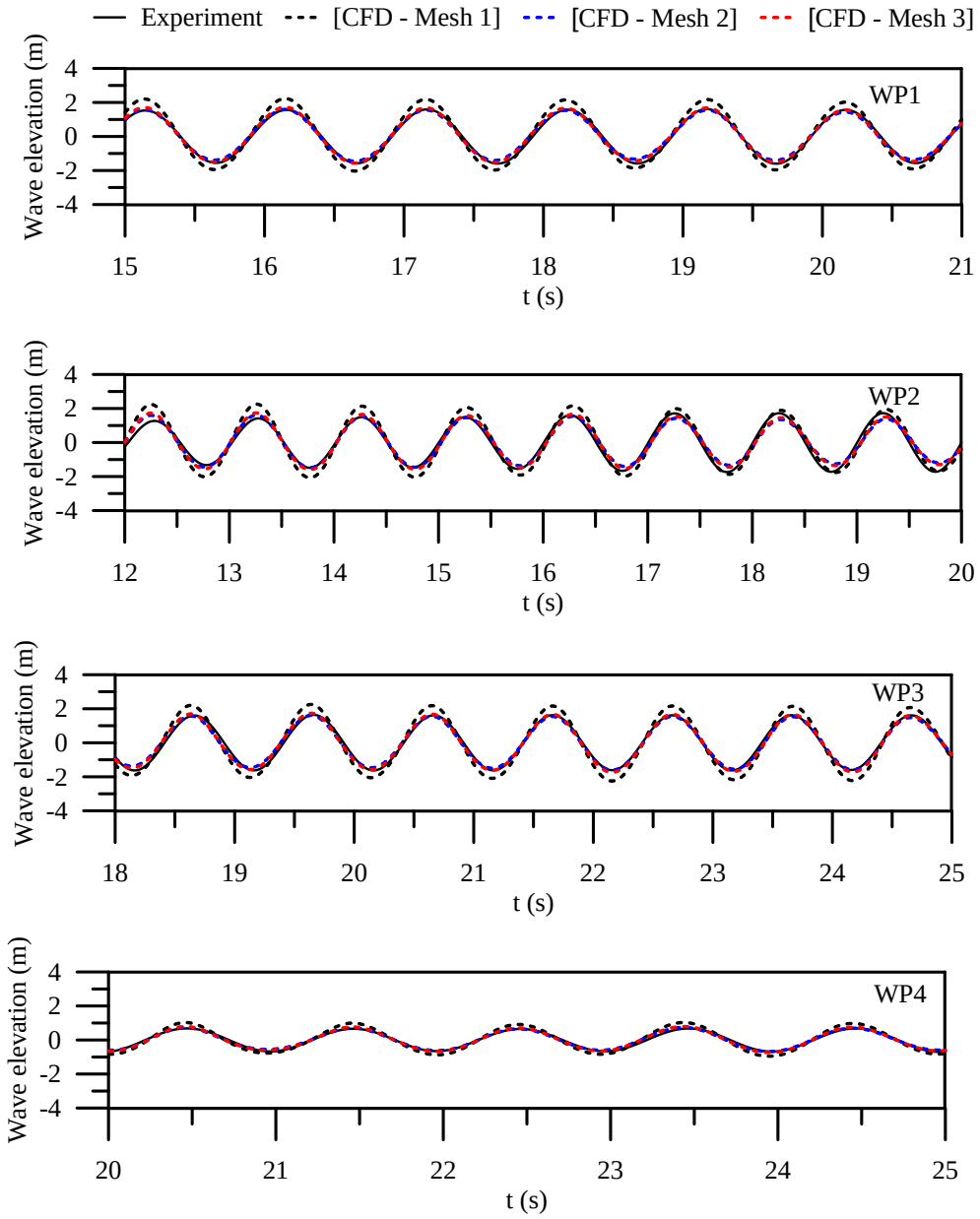

Fig. 4 Comparison of time history of free-surface wave elevations between CFD and experimental results at different wave probes according to Mesh-types

Table 2 Tested parameters of wave and porous barrier

		Case 1	Case 2
Wave parameters	Wave steepness, H/λ	0.01	0.02
	Period (s)	1.0	
Type		Rigid	Porous
Barrier	Length, a (m)	0.8	
	Thickness, b (mm)	2	
	Porosity, P	0.0	0.0567 (c = 12 mm, r = 3 mm)

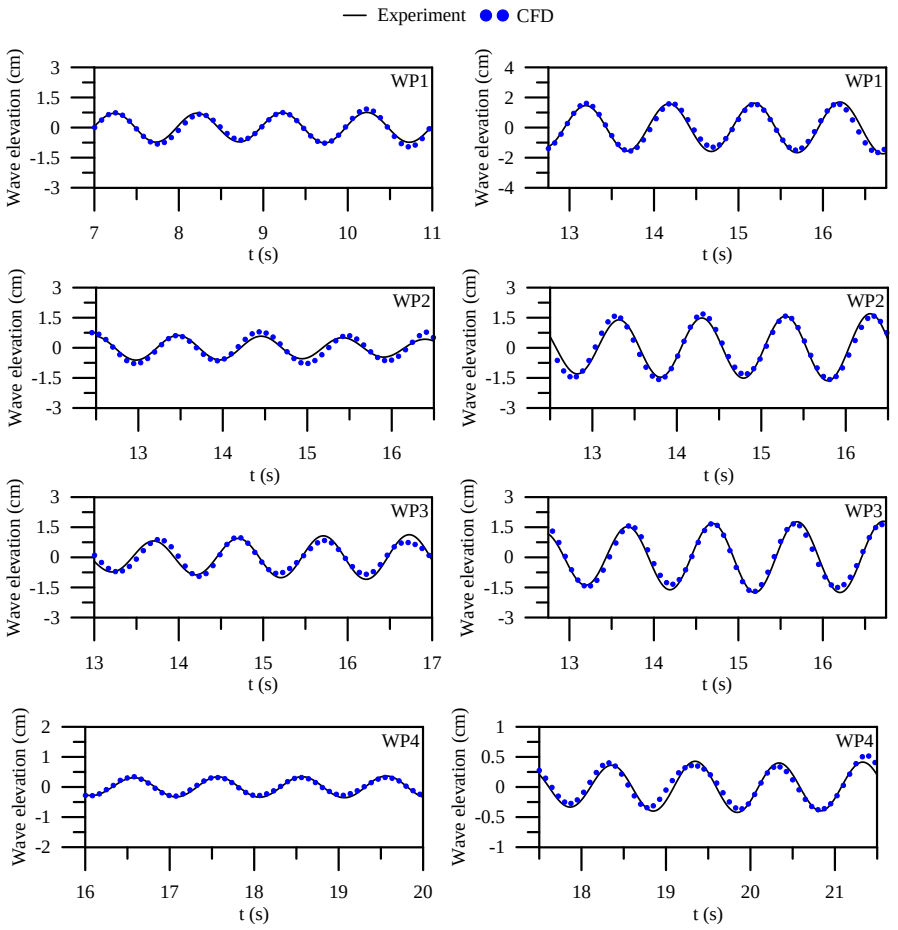

Fig. 5 Comparison of time history of free-surface elevation between CFD and experimental results at different wave probes for (a) $P = 0.0$, $H/\lambda = 0.01$ (b) $P = 0.0567$, $H/\lambda = 0.02$

Table 3 Comparison of measured and calculated reflection and transmission coefficients for different porous barriers

		R_f	T_r
Case 1	Experiment	0.747	0.478
	CFD	0.718	0.468
Case 2	Experiment	0.451	0.266
	CFD	0.441	0.283

4.3 Reflection and transmission coefficients

Fig. 6 shows the CFD results, along with the experimental results for different porosities of $P = 0.0567, 0.1275$, and 0.2267. The predicted CFD solutions follow properly the trend of the experimental results, regardless of the porosity. The reflection R_f and energy-loss coefficients $\varepsilon(=1-R_f^2-T_r^2)$ increase with an increase in kh, whereas the transmission coefficient T_r shows a contrary trend. As the barrier porosity increases, the reflection coefficient decrease, however, the transmission coefficient does not change significantly. The energy loss across a horizontal porous barrier is greatest at the porosity of $P = 0.1275$. It means there exist an optimal value of porosity for maximum energy dissipation. Irrespective of the porosity of a horizontal porous barrier, the horizontal porous barrier is more effective in dissipating the energy in short period waves than in long-period waves. Additionally, as kh approaches zero, incoming waves are fully transmitted through the porous barrier. Overall, a close agreement of R_f, T_r, and ε between the experimental and CFD results were noted.

To shed a deeper understanding of the complex flow physics of the propagating wave over the horizontal porous barrier, the snapshots of the computed wave profile around the porous plate were presented for different porosities. Accordingly, rigid ($P = 0.0$) and three different porous barriers ($P = 0.0567, 0.1275$, and 0.2267) were chosen for a given wavelength ($kh=2.5$) and wave steepness ($H/\lambda = 0.02$ and 0.04). A snapshot was taken at time instant (t = 3.96 sec) and shown in Fig. 7. When a wave propagates toward the barrier, a sudden change in the water depth forces the wave profile to likely adjust to the local conditions by steepening the wave with a shorter wavelength and higher wave heights (commonly known as wave shoaling). Eventually, the crest ultimately curls forward and forms a jet plunging into the trough ahead; this type of breaker is called a plunging breaker (see Fig. 7). Once the wave breaks, the strong nonlinear interaction and turbulence mixing occur over the barrier. Two strong tip vortices at both ends of the barrier moving in opposite directions to each other were observed. The intensity of the tip vortices is higher for the rigid barrier and less for the porous barriers. However, the porous barriers generate the small-scale vortices associated with jet flow through the small holes. A barrier with a high porosity ($P = 0.2267$) shows higher velocity magnitudes through the holes than the other two porosities ($P = 0.0567$ and 0.1275). Stronger vertical forces were noted in the rigid barrier, but they were nullified by forming strong jet flow through the holes at the porous barrier. The wave run-up, tip vortex, and jet flow were considerably stronger when the wave steepness increases up to $H/\lambda = 0.04$.

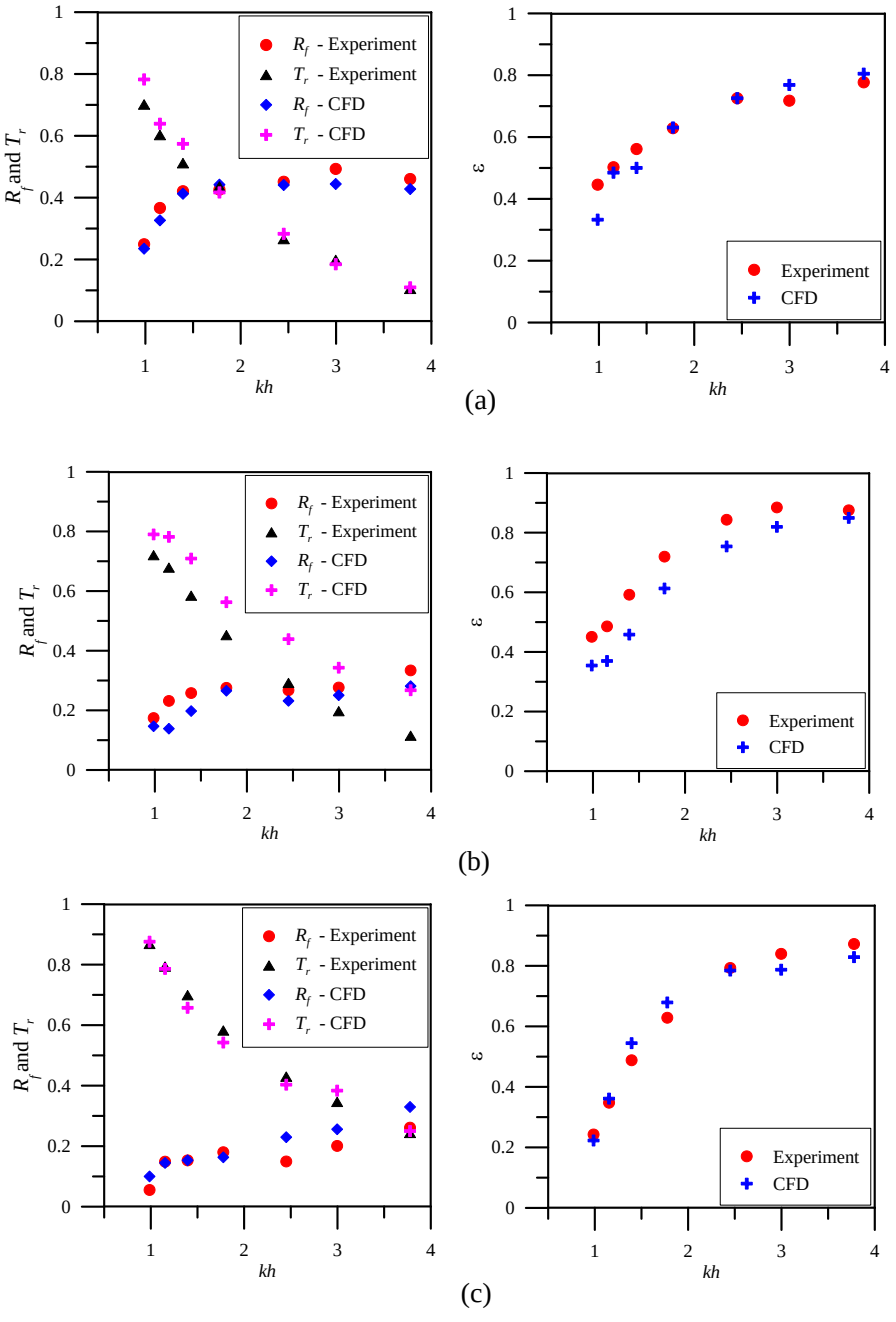

Fig. 6 Comparison of reflection, transmission, and energy-loss coefficients as a function of non-dimensional wavelengths and porosities at a fixed wave steepness ($H/\lambda = 0.02$) (a) $P = 0.0567$, (b) $P = 0.1275$, and (c) $P = 0.2267$

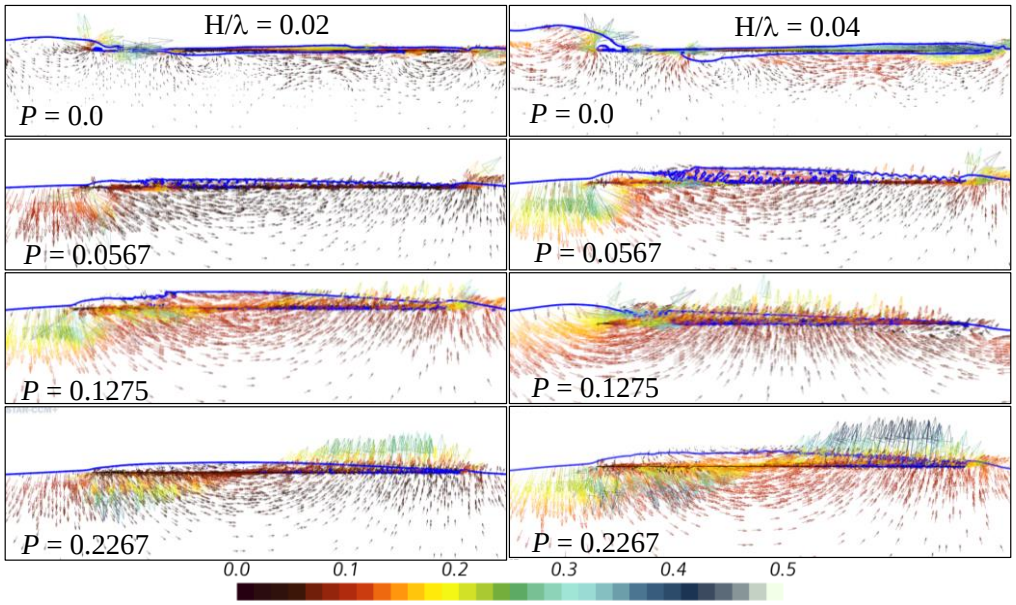

Fig. 7 Velocity vector field around the surface-fixed horizontal barrier with different porosities and wave steepness

Overall, the total energy dissipation is augmented with the wave run-up, wave breaking, free surface fragmentation, small jet flow, and vortex generation at the tips of the porous barriers.

4.4 Vertical wave force

To quantify the nonlinear wave force experienced by the porous barriers with the same parameters as Fig. 7, Figs. 8 and 9 show the time history of the vertical wave force. The time history of wave force shows that the increase in barrier porosity slowly reduces the wave force.

For a quantitative assessment of nonlinear wave force, Fourier decomposition was performed to extract the higher harmonics. The present study only retains the first three harmonic components. Indeed, Figs. 8 and 9 show that intrinsic nonlinearity provides a mechanism in converting energy from first to higher harmonics. The rate of energy conversion to higher harmonics increases with the increase in porosity for both the wave steepness. This phenomenon could be attributed to the increase in frictional loss enervated through the holes. Consequently, the total vertical force decreases with an increase in porosity of the barrier. The vertical wave force tends to increase the nonlinearity with the increase in wave steepness from $H/\lambda = 0.02$ to $H/\lambda = 0.04$ (see Fig. 9).

In addition, the vertical wave force estimation could be extended to other values of kh as shown in Fig. 10 for four different porosities ($P = 0.0, 0.0567, 0.1275$ and 0.2267). Fig. 10 excludes the experimental data, and the analytical solution is cited from Linton's work (2001) for comparison of a rigid barrier. The analytical solution provided by Linton is based on matched eigenfunction expansions and residue calculus theory. Fig. 10(a) presents the CFD solution together with the analytical solution for the rigid barrier, whereas Fig. 10(b) shows the CFD solution for the porous

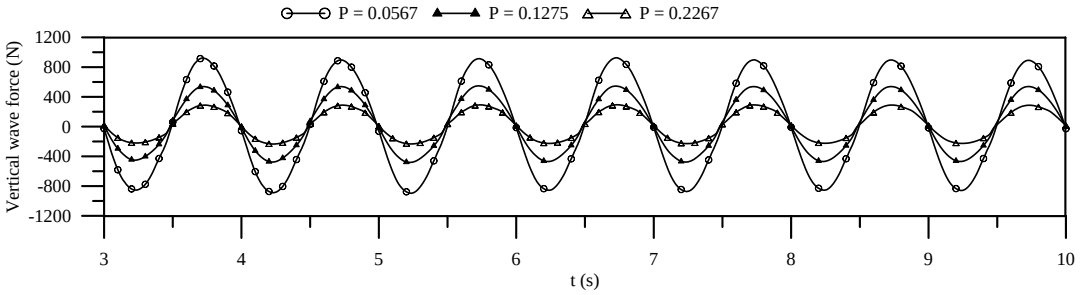

(a)

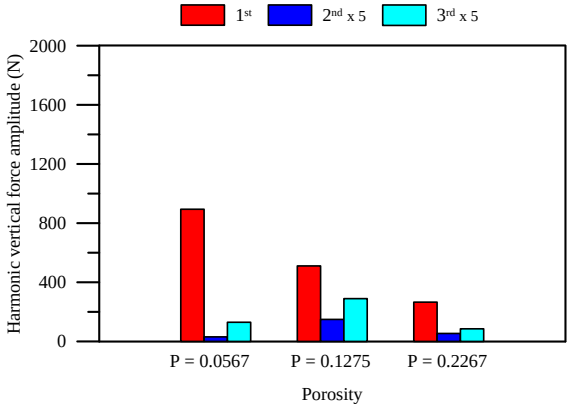

(b)

Fig. 8 Time history and first three harmonics of vertical wave force on the barriers with different porosities for $H/\lambda = 0.02$

barrier with different porosities (see Fig. 10(b)). Notably, the agreement in Fig. 10(a) appears to be good between CFD and Linton's results. The barrier with porosity of $P = 0.1275$ generally shows the lowest force estimation among other porosities (see Fig. 10(b)). With the increase in kh, the wave forces exerted on the porous barrier also decrease significantly. Porous barriers with different porosities show higher force in the long-period region and decrease as kh goes to higher values.

5. Conclusions

The present study has been investigated experimentally and numerically for interaction of monochromatic waves with a surface-fixed horizontal porous wave barrier, by considering varying barrier porosities and non-dimensional wavelengths. The laboratory experiments were carried out in a 2D wave tank at Jeju National University. The porous barriers with different porosities were manufactured by varying the distance between the holes arrayed in a staggered manner with a fixed diameter of the hole. A 3D NWT computation was performed on the basis of incompressible viscous fluid governed by RANS equations.

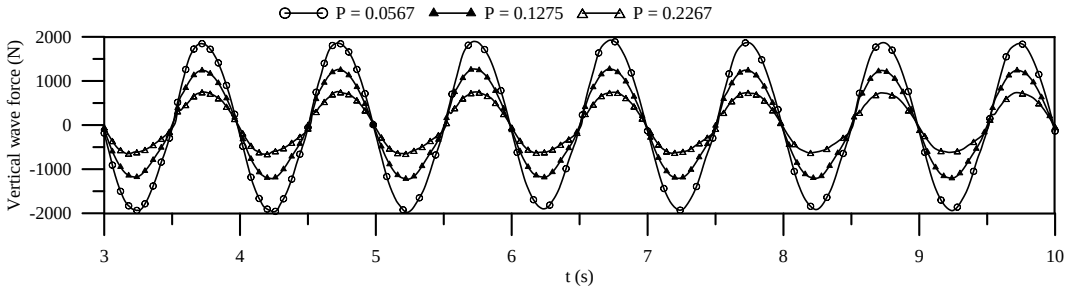

(a)

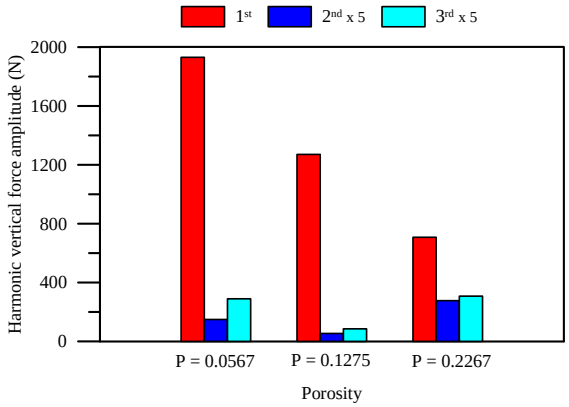

(b)

Fig. 9 Time history and first three harmonics of vertical wave force on the barriers with different porosities for $H/\lambda = 0.04$

After the initial mesh convergence test, numerical validation for mesh generation was achieved by comparing the experimental results. The time history of free-surface wave elevation calculated at different positions of wave probes was compared with the experimental results for given wave conditions and porous barriers of porosities $P = 0.0$, and 0.0567. Subsequently, the reflection and transmission coefficients between the CFD and experimental results were compared for different porosities $P = 0.0,\ 0.0567,\ 0.1275,$ and 0.2267. Regardless of kh values, the calculated CFD solutions of R_f, T_r and energy-loss coefficient ε effectively predict the measured experimental results. The surface-fixed horizontal barrier is more effective in dissipating wave energy in the short wave period region and has an optimal porosity value near $P = 0.1$.

From the snapshot of the wave profile, the presence of a surface-fixed horizontal porous barrier tends to steepen the waves over the horizontal barrier due to wave shoaling. Some amount of wave energy is dissipated through the wave breaking, jet flow, and vortex formation at the tips and small holes, and these phenomena are accelerated by increasing the wave steepness. The intensity of the tip vortex at both ends of the barrier is stronger for the rigid barrier and less for the porous barriers including vortex generation associated with jet flow through the small holes.

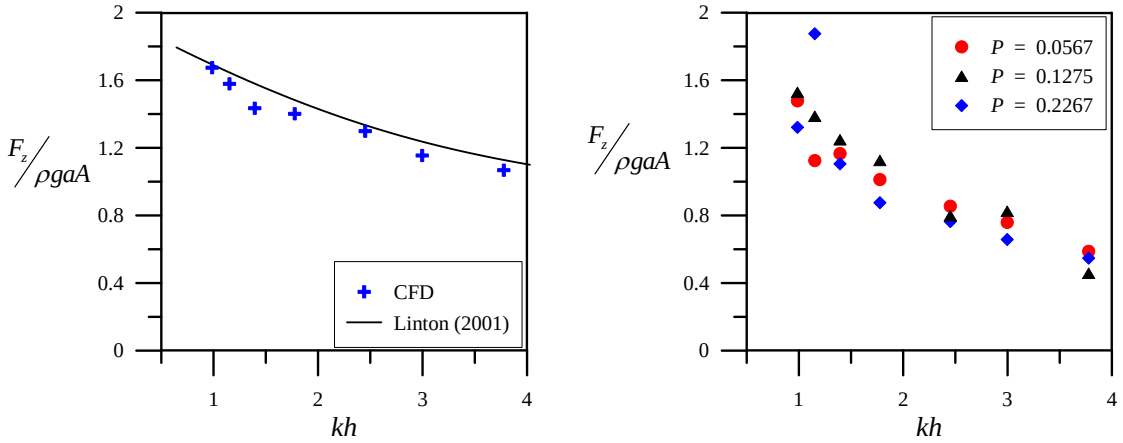

Fig. 10 Non-dimensional vertical wave force versus kh for $H/\lambda = 0.02$ (a) Rigid barrier and (b) Porous barriers

To investigate the nonlinearity quantitatively from the time series of wave force, a discrete Fourier harmonic decomposition was performed. The more energy conversion was observed from the first harmonic to higher harmonics with the increase in porosity. Finally, the CFD solutions on the rigid barrier were compared with the Linton's analytical solution (2001). Notably the comparison showed good agreement. The CFD results of vertical wave force revealed that wave vertical force decreases with an increase of barrier porosity, as expected.

Acknowledgments

This research was supported by the 2021 scientific promotion program funded by Jeju National University, South Korea.

References

An, S. and Faltinsen, O.M. (2012), "Linear free-surface effects on a horizontally submerged and perforated 2D thin plate in finite and infinite water depths", *Appl. Ocean Res.*, **37**, 220-234.

Cho, I.H. and Kim, M.H. (2008), "Wave absorbing system using inclined perforated plates", *J. Fluid Mech.*, **608**, 1-20.

Cho, I.H. and Kim, M.H. (2013), "Transmission of oblique incident waves by a submerged horizontal porous plate", *Ocean Eng.*, **61**, 56-65.

Chwang, A.T. and Chan, A.T. (1998), "Interaction between porous media and wave motion", *Annu. Rev. Fluid Mech.*, **30**(1), 53-84.

Crowley, S. and Porter, R. (2012), "The Effect of Slatted Screens on Waves", *J. Eng. Math.,* **76**, 53-76.

Enger, S., Peric, M. and Monteiro, H. (2014), "Coupling of 3D numerical solution method based on Navier-Stokes equations with solutions based on simpler theories", *Proceedings of the XXXV Iberian Latin-American Congress on Computational Methods in Engineering*, ABMEC Fortaleza, CE, Brazil.

Evans, D.V. and Peter, M.A. (2011), "Asymptotic reflection of linear water waves by submerged horizontal

porous plates", *J. Eng. Math.,* **69**(2-3), 135-54.
Laws, E.M. and Livesey, J.L. (1978), "Flow through screens", *Annu. Rev. Fluid. Mech.*, **10**(1), 247-266.
Linton, C.M. (2001). "The finite dock problem", *Zeitschrift für angewandte Mathematik und Physik ZAMP*, **52**(4), 640-656.
Liu, Y. and Li, Y.C. (2011), "An alternative analytical solution for water-wave motion over a submerged horizontal porous plate", *J. Eng. Math.*, **69**, 385-400.
Mansard, E.P. and Funke, E.R. (1980), "The measurement of incident and reflected spectra using a least squares method", *Proceedings of the 17th International Conference on Coastal Engineering Coastal Engineering*.
Mei, C.C., Liu, P.L. and Ippen, A.T. (1974), "Quadratic loss and scattering of long waves", *J. Waterw. Harbors Coast. Eng. Div.*, **100**(3), 217-239.
Molin, B. and Nielsen, F.G. (2004), "Heave added mass and damping of a perforated disk below the free surface", *Proceedings of the 19th international workshop on water waves and Floating bodies*.
Molin, B., Remy, F. and Rippol, T. (2008), "Experimental study of the heave added mass and damping of solid and perforated disks close to the free surface", *Maritime industry, ocean engineering and coastal resources,* Taylor & Francis, 879-887.
Molin, B. (2011), "Hydrodynamic modeling of perforated structures", *Appl. Ocean Res.*, **33**, 1-11.
Molin, B. (1992), "*Motion damping by slotted structures*", (Ed., van den Boom, H.J.J.), Hydrodynamics: computations, model tests and reality. Developments in marine technology, vol. 10. Elsevier, 297-303.
Park, W.T., Lee, S.H., Kee, S.T. and Park, J.K. (2005), "Submerged porous plate wave absorber", *Proceedings of the 15th International Offshore and Polar Engineering Conference. International Society of Offshore and Polar Engineers*.
Patarapanich, M. and Cheong, H.F. (1989), "Reflection and transmission characteristics of regular and random waves from a submerged horizontal plate", *Coast. Eng.*, **13**(2), 61-182.
Peric, M. (2017), "Best practices for flow simulations with waves", *Star global conference*, Berlin.
Poguluri, S.K. and Cho, I.H. (2020). "Wave dissipation over a horizontal slotted plate with a leeside vertical seawall: Analytical and numerical approaches", *Coast. Eng. J.* (In Press).
Seiffert, B., Hayatdavoodi, M. and Ertekin, R.C. (2014), "Experiments and computations of solitary-wave forces on a coastal-bridge deck. Part I: Flat plate", *Coast. Eng.*, **88**, 194-209.
Siew, P.F. and Hurley, D.G. (1977), "Long surface wave incident on a submerged horizontal plate", *J. Fluid Mech.*, **83**, 141-151.
You, R., He, G., Wang, J. and Liu, P. (2019). "CIP-based analysis on strongly nonlinear interaction between solitary wave and submerged flat plate", *Ocean Eng.*, **176**, 211-221.
Yu, X. and Chwang, A.T. (1994), "Water waves above submerged porous plate", *J. Eng. Mech.,* **120,** 1270–81.
Yu, X. (2002), "Functional performance of a submerged and essentially horizontal plate for offshore wave control: a review", *Coast. Eng. J.*, **44**(2), 127-147.
Yu, X. (1995), "Diffraction of water waves by porous breakwaters", *J. Waterw. Port Coast. Ocean Eng.*, **121**(6), 275-282.

MK